X-Ray Telescopes

X-ray telescopes produce images of x-ray-emitting objects within the telescope's FIELD OF VIEW by reflection from precisely shaped mirrors. Hans Wolter's design in the early 1950s of an x-ray microscope using reflective optics led Riccardo GIACCONI to suggest an 'inverted' set of optics, not subject to the fabrication limitations of the microscope, could be used as a cosmic x-ray telescope. As described in 1960 by Giacconi and Bruno ROSSI, imaging with x-ray telescopes offers a significant reduction in noise, both from cosmic ray induced events and the soft x-ray background. This is because most background counts are the result of charged particles and are uniformly distributed over the detector area. An imaging system concentrates the source counts in one or a few pixels. As an example, the EINSTEIN (HEAO-2) Observatory x-ray telescope offered an improvement in sensitivity of about a factor of 1000 over that of the large-area, collimated proportional counters on High Energy Astrophysical Observatory (HEAO) 1 satellite. The improved instrument sensitivity resulting from increased signal to noise enables the study of fainter sources, extending the number and age of detectable objects.

Imaging observations enable deeper study of extended cosmic x-ray sources. Imaging of CLUSTERS OF GALAXIES reveals details of the intracluster gas temperature profile and isolates the x-ray emission from component galaxies. Imaging of GALAXIES allows study of any central source as well as the identification and location of the galactic emitters. Study of SUPERNOVA REMNANTS allows the visualization of the x-ray-emitting regions and potential identification of a remnant's compact object. None of these types of studies is readily undertaken with non-imaging instruments. Other imaging approaches employing such devices as modulation collimators or scanned, tightly collimated detectors provide much poorer resolution ($\sim$1 arcmin.) than that available with current x-ray telescopes and suffer from image reconstruction artifacts.

Studies of point sources also benefit from x-ray telescope resolution. Using the large-area proportional counters on board HEAO-1, positions accurate to $\sim$0.1 square degrees were obtained for weak point sources. On average, there will be one star brighter than 12th magnitude in the position error box. For comparison, the optical counterparts of Sco X-1 and Cen X-1 are about 13th magnitude, and that of Her X-1 about 15th magnitude. Imaging enables more accurate optical identifications. With better than 0.5 arcsec resolution of the Chandra X-ray Observatory (CXO) positions of point sources accurate to $\sim$10^{-7} square degrees may be obtained—on average less than a single unrelated 20th magnitude star will be found in the error box.

This article will first briefly discuss how x-rays may be reflected and what optical systems can be used to form images. Key considerations for performance and system design will be discussed, followed by the various ways of implementing x-ray telescopes. We will review the more significant past and current x-ray telescopes, and then discuss future trends in x-ray telescopes.

X-ray reflectance

X-rays specularly reflect from a surface under two conditions, when striking a surface at grazing incidence and when constructive interference takes place between many layers of a material whose atomic number varies in a periodic fashion.

Reflection at grazing incidence

At x-ray wavelengths the real part n_r of the complex index of refraction $n_r - ik$ of the reflecting surface is less than 1. Thus x-rays in vacuum are incident upon an interface that is less optically dense. From Snell's law the angle of the wave transmitted θ_t into the less dense material is

$$\sin \theta_t = (n_1/n_2) \sin \theta_i \tag{1}$$

where θ_i is the angle of incidence and n_1 and n_2 are the indices of refraction for vacuum and the reflecting material, respectively. When $n_1 > n_2$ one obtains a real value for θ_t only for incident angles $\theta_i < \sin^{-1}(n_2/n_1)$. For example, if $n_2 = 0.99$, then the maximum real value for θ_i is 81.9°: at this incident angle the transmitted angle is 90°, parallel to the interface. For larger incident angles (shallower grazing angles) no radiation is transmitted. This is seen by allowing θ_t to be complex, with

$$\cos \theta_t = \pm i[(n_1/n_2)^2 \sin^2 \theta_i - 1]^{1/2}. \tag{2}$$

Substituting equation (2) into the Fresnel equations, solving for the transmitted electric and magnetic fields, and determining the time-averaged Poynting vector reveals that no energy flows through the interface—the field intensities normal to the interface decay exponentially into the less optically dense surface.

Reflectance is calculated from the complex index of refraction using the Fresnel equations. The real and imaginary parts of the index are computed from the atomic (forward) scattering factors f_1 and f_2:

$$n_r = 1 - \delta = 1 - \frac{\rho}{W_m} A_0 r_e \lambda^2 f_1 \frac{1}{2\pi}$$

$$k = \frac{\rho}{W_m} A_0 r_e \lambda^2 f_2 \frac{1}{2\pi} \tag{3}$$

where ρ is the material density, W_m is the molar weight of the reflecting material, A_0 is Avogadro's number, r_e is the classical electron radius and λ is the incident wavelength. The scattering factors are material and wavelength dependent. They are derived in a variety of ways: they may be computed from measurement of the forward scattering amplitude or back calculated from measured x-ray reflectance. Well-known sets of constants have been published by Henke *et al*, Auerbach and Tirsell, and Windt. As better reflectance is achieved with materials with high electron density grazing incidence optics are typically coated with metals to enhance reflectance.
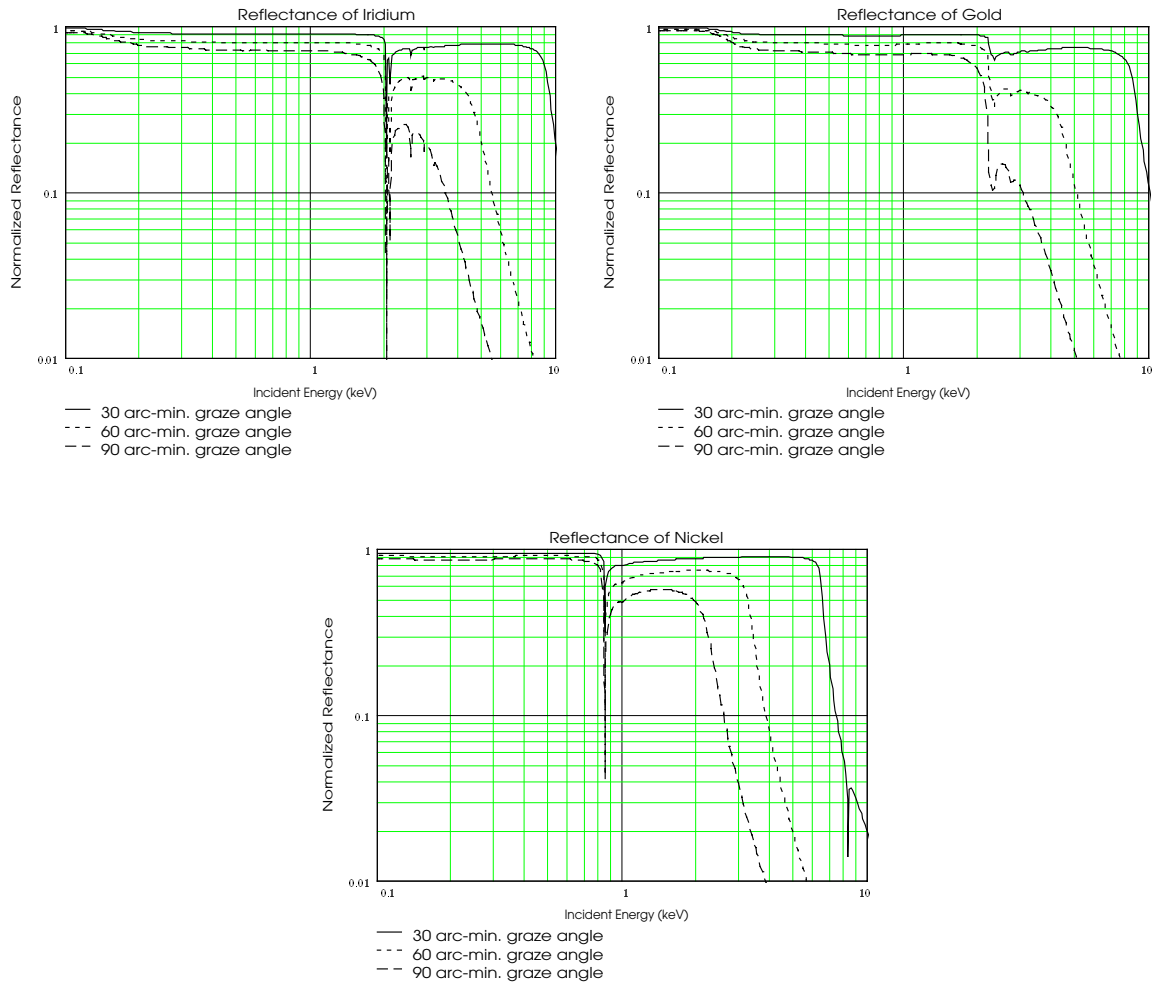
Figure 1. X-ray reflectance as a function of incident energy and graze angle.

Common materials used as reflecting coatings are iridium, gold and nickel. A plot of x-ray reflectance as a function of incident energy and grazing angle is shown in figure 1. Note the local minima in reflectance at the location of x-ray absorption edges. The product of reflectance and geometric collecting area (the entrance aperture) is called the effective area. Reflectance decreases as a function of increasing graze angle and starts to decrease rapidly near the so-called critical angle. The critical angle may be expresses as $\cos^{-1}(n_r) \approx (2\delta)^{1/2}$ for $\delta \ll 1$ (see equation (3)).

Reflection from multilayer coatings
Multilayer coatings contain alternating layers of high-Z (atomic number) and low-Z materials. Reflection occurs at each interface, and the layer optical thicknesses are chosen so as to produce constructive interference between each layer. Reflection occurs only for those wavelengths which satisfy the Bragg equation,

$$m\lambda = d\sin\theta \qquad (4)$$

where d is the layer spacing and θ is the incident angle. In practice the coating reflects a bandwidth $\Delta\lambda$ that is a function of various fabrication parameters including layer thickness uniformity, density, and layer materials but is typically only a few ångströms wide. Typical layer material pairs include (but are not limited to) nickel/carbon, tungsten/silicon, rhodium/beryllium, rhodium/carbon, molybdenum/carbon and platinum/carbon. A typical coating may contain between 40 and 500 layer pairs, with the larger number of layers yielding higher reflectance. Reflectance of 10–80% has been achieved, depending on the incident wavelength (higher reflectance at longer wavelengths) and material choices.

Several soft x-ray–EUV, normal incidence, multilayer telescopes have been launched on board sounding rockets and small satellites, including the recently launched Transition Region and Corona Explorer (TRACE). To overcome the spectral bandwidth limitations of multilayer coatings, experimenters have resorted to integrating several smaller telescopes into a single payload, each telescope with a different multilayer. In

the case of TRACE, different multilayer coatings were applied to each of the four quadrants of the optics so that a single telescope was sensitive to four separate spectral bandwidths (one of which was visible light).

An alternative to several different telescopes or multiple different coatings on a single telescope is graded multilayers, or 'supermirrors'. Here, the layer thickness varies as a function of position (depth) in the layer stack. The thickest layers are at the top of the stack to reflect the longest wavelengths with a minimum of absorption. Good broadband reflectance has been achieved using a thickness law

$$d_i = a(b + i)^{-c} \qquad (5)$$

where d_i is the thickness of the ith layer (starting from the top), a and c are positive parameters that are a function of the materials used, and b is a constant greater than -1.

Substrate and coating roughness degrades multilayer performance. 'Low' frequency roughness ($>1\,\mu$m periods) causes scatter which degrades image contrast. 'High' frequency roughness ($<1\,\mu$m periods) reduces reflectance.

Types of telescopes

Two approaches are used to achieve imaging: grazing incidence (GI) and normal incidence (NI). Grazing incidence telescopes utilize large angles of incidence (near $90°$) so that the x-rays graze or glance off the surface and are reflected. Normal incidence x-ray telescopes use more conventional shaped optics with multilayer coatings.

Grazing incidence telescopes

In 1952 the German physicist Hans Wolter was able to show that a two-element system containing an even number of confocal conic optics will come close to satisfying the Abbe sine condition; rays that reflect off both surfaces are focused and form an image. Wolter, attempting to produce systems for x-ray microscopy, produced three designs, referred to as Wolter types I, II and III. The type I telescope (figure 2) consists of a paraboloid as a primary mirror and a confocal and coaxial hyperboloid as the secondary mirror. The paraboloid focus is coincident with the back hyperboloid focus. X-rays strike the paraboloid at the grazing angle (approximately the field angle of the source plus half the angle subtended by the best-fit cone to the paraboloid), are reflected and strike the hyperbola. The image is formed at the front hyperboloid focus. Usually, the hyperboloid cone angle is three times that of the paraboloid so that on-axis x-rays are incident upon both mirrors with essentially the same grazing angle. X-rays that strike the forward end of the paraboloid reflect to strike the aft (back) end of the hyperboloid, and vice versa.

The entrance aperture is the projection of the primary mirror in the aperture plane. This results in an annular aperture whose width is approximately the product of the optic length and the half-angle of the best fit cone (the cone angle). For the CXO the largest paraboloid has a surface area of approximately 3.2 m^2 but an entrance aperture of only 0.047 m^2, a reduction of a factor of
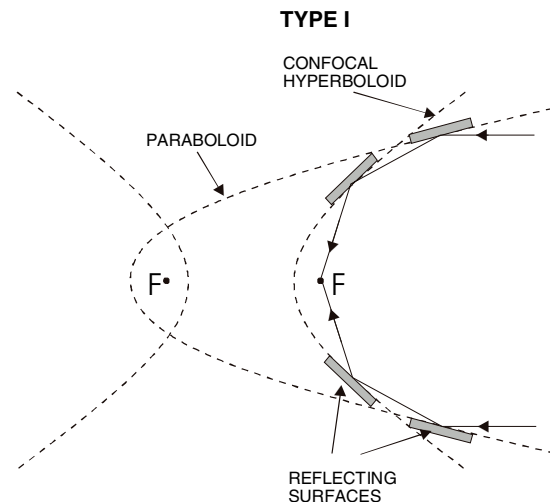

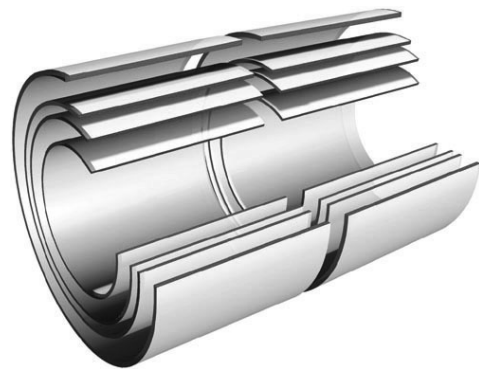**Figure 2.** Schematic representation of the Wolter type I telescope.

Figure 3. Cutaway schematic drawing of the nested four shells (paraboloid and hyperboloids) of the Chandra X-ray Observatory (courtesy of the Raytheon Co).

~68 times. Collecting area is built up by nesting mirror pairs within one another (figure 3). Each mirror pair, or shell, is co-aligned and confocal. The telescope entrance aperture consists of a set of concentric annular apertures, all contributing to the same focus. Ideally, the shells are designed so that each one has the same focal length and therefore the same plate scale (the proportionality constant relating angular distance on the sky to linear distance at the focal plane). All shells do not necessarily contribute the same to the image as a function of x-ray energy. As shown above in the section 'X-ray reflectance', reflectance is a function of graze angle and incident energy. The inner shells have a shallower graze angle than outer shells. Thus the inner shells of a nested telescope have a larger spectral bandwidth (reflect higher-energy x-rays) and comparable or slightly higher reflectance than the outer shells, while also having a smaller entrance aperture.

The type I design yields a perfect image for on-axis illumination. Off axis, the design suffers from field dependent coma and spherical aberration. In addition,
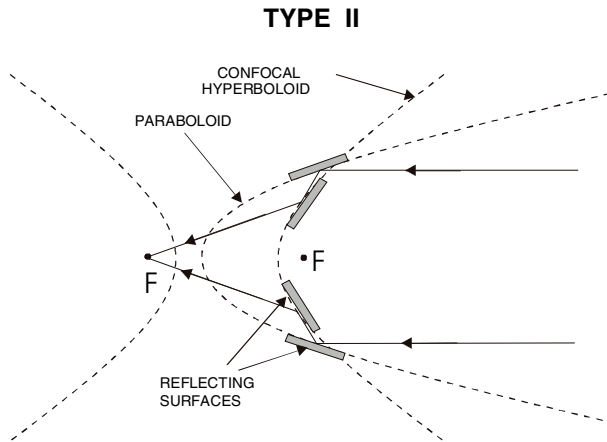
3

TYPE II

Figure 4. Schematic representation of the Wolter type II telescope.

the telescope focal surface is curved. Van Speybroeck and Chase (1972) approximated the off-axis rms blur diameter for a flat focal plane detector at the Gaussian focus as

$$\sigma_{\text{blur}} \approx 4\frac{\xi+1}{10}\frac{(\tan\theta_{\text{field}})^2}{\tan\alpha}\frac{L}{Z_0} + 8\tan(\theta_{\text{field}})(\tan\alpha)^2 \quad (6)$$

where θ_{field} is the field angle (the off-axis angle), α is the graze angle, Z_0 is the axial distance from the intersection of the paraboloid and hyperboloid surfaces (the 'virtual joint') to best on-axis focus, and L is the axial length of the paraboloid. The first term in equation (6) represents the field-dependent coma. The second term is split between a GI equivalent of spherical aberration and image defocus (relative to a flat detector) due to a curved focal surface. For the Chandra X-ray Observatory at a field angle of 5 arcmin, the rms blur diameter ranges from 2.5 arcsec to 4 arcsec. Alternative Wolter I type designs exist that mitigate the off-axis aberrations at the expense of degrading on-axis performance. These designs consist of using two coaxial (but not confocal) hyperboloids or using generalized (non-conic) mirror prescriptions such as a power law. Because of the relative mechanical simplicity of the design and the ability to increase collecting area by nesting telescopes the type I design (or its variants) is the most common form of grazing incidence designs used in x-ray astronomy, being employed on the Einstein Observatory, Roentgen Satellite (ROSAT), CXO, X-ray Multi-mirror Mission (XMM) and many others described later.

The type II design also consists of a grazing incidence paraboloid primary and hyperboloid secondary mirror, but the outer surface of the hyperboloid is used, as shown in figure 4. In the type II the image is formed at the back hyperboloid focus. Type II telescopes enable longer focal lengths than a type I with comparable grazing angle and entrance aperture, affording an increased plate scale. Field-angle-dependent aberrations are greater with type II designs than with type I designs. Also, nesting of telescopes to increase collecting area is impractical.

Instead, collecting area may be increased by increasing the grazing angle, thereby increasing the projected area on the aperture plane, while maintaining a usefully long focal length and acceptable plate scale. The increase in graze angle, however, limits the useful spectral bandwidth of the telescope so that most practical type II telescopes are used for the extreme to far ultraviolet and longer wavelengths (>100 Å).

The type III design employs the outer surface of a paraboloid as the primary element and the inner surface of an ellipsoid as the secondary mirror. The paraboloid focus is coincident with one of the ellipsoid foci, and the image falls upon the other ellipsoid focus. The type III design has never been used for x-ray astronomy.

Wolter developed variants of the original designs by extending results obtained by Karl SCHWARZSCHILD in 1905 for normal incidence telescopes. The modified prescriptions are called Wolter–Schwarzschild (W–S) designs and differ slightly in their second-order figure (shape). These optics satisfy the Abbe sine condition strictly and so do not exhibit any comatic aberration. The improvement in off-axis performance of W–S designs over conventional designs is graze angle dependent. Thus W–S designs provide negligible improvement at the shallow graze angles (<1°) employed on many x-ray telescopes to achieve good reflectance at shorter wavelengths. W–S-type designs have been used on a number of extreme ultraviolet telescope applications which use much larger graze angles (>5°). The EXTREME ULTRAVIOLET EXPLORER (EUVE) contained a W–S type I EUV telescope and a W–S type II for the stellar spectrometer. ROSAT, besides carrying the large Wolter I x-ray telescope, also carried a W–S type I EUV telescope—the Wide Field Camera—which had a 5° field of view, ∼450 cm^2 aperture and image half-power diameter of ∼1.7 arcmin (on axis).

Contamination of the optical surface will degrade performance. Particulates both absorb and scatter the x-rays, degrading the point spread function and reducing the effective collecting area. Hydrocarbons absorb x-rays. Grazing incidence telescopes are extremely sensitive to both. This is a direct result of the shallow grazing angle, as can be seen in figure 5. A round particle of cross section πa^2 maps onto an entrance aperture area of $2\pi a^2$ because x-rays may strike the particle before or after reflecting off the mirror surface. The mirror surface area is $2\pi RL$ where R is the average radius of the nearly conical optic. The mirror entrance aperture has an area of $2\pi RL\sin\alpha$. Thus the fraction of mirror surface area F_n covered by the particle is

$$F_n = \frac{\pi a^2}{2\pi RL} \quad (7)$$

but the fraction of the entrance aperture F_A 'covered' by the particle is

$$F_A = \frac{2\pi a^2}{2\pi RL\sin\alpha} = F_n\frac{2}{\sin\alpha} \quad (8)$$

For a 1° graze angle F_A is ∼114 times larger than F_n. Similarly for a hydrocarbon layer t thick, the x-rays
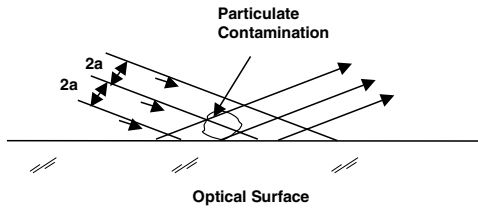
Figure 5. Illustration of the effects of particulate contamination. Incident x-rays from the upper left are absorbed or scattered by the particle either when directly impinging upon it or when impinging upon it after reflection from the mirror.

must traverse a distance $2t/\sin\alpha$. In addition, because of their construction with little space between telescope shells and very narrow entrance and exit annuli, it is extremely difficult to clean a dirty grazing incidence optic. Contamination control is a critical issue for grazing incidence optics.

Finally, an earlier realization than the Wolter designs was the Baez–Kirkpatrick telescope in which an array of parallel plates, parabolic in the plane of incidence, focus the incident x-rays to a line image. Placing a second set of plates oriented at a right-angle to the first set focuses the line image to a point image. This design has more aberrations than the Wolter designs, but may be approximated using optically flat plates bent in one axis so as to inexpensively build up large collecting area with moderate resolution.

Multilayer telescopes
Conventional optical telescope designs, when used as the substrate for multilayer coatings, are suitable for x-ray telescopes. The distinction between normal incidence x-ray and optical telescopes is that optical telescopes are diffraction limited and x-ray telescopes (to date) are not. To achieve diffraction-limited performance, the telescope wavefront error must be less than $\sim\lambda_x/13$, rms, where λ_x is the x-ray wavelength. For a two-mirror system being used at 171 Å, this equates to a surface error figure of $\sim$5 Å, rms, or better than $\lambda/1300$ ($\lambda = 633$ nm), rms (neglecting other error contributors such as mirror figure degradation due to coating, support deformation, misalignments, etc). The ability to manufacture such optics is only starting to be feasible at the end of 1999. In addition, because of the short wavelength (relative to visible light) and current detector technology, extremely long focal lengths (>10 m) are required to make use of diffraction-limited performance.

Mechanical stresses in the multilayer coating can produce deformations of the optic, degrading imaging. Recent studies have shown that the stresses do not appear to vary as a function of the layer pair thickness, but do vary as a function of the equivalent d thickness and the materials. Thin-film technologists have found that coating stresses are also functions of a number of deposition parameters including substrate temperature and deposition process. Thin-film stresses may be estimated from Stoney's equation:

$$\sigma_f = \frac{E_s t_s^2}{6(1-\nu_s)t_f}\,\Delta C \tag{9}$$

where E_s, ν_s and t_s are, respectively, Young's modulus, the Poisson ratio and the thickness of the substrate, t_f is the thickness of the coating, ΔC is the change in radius of curvature of the substrate after the coating is applied and σ_f is the induced stress (a negative value of σ_f is compressive). Typical stresses range from -1200 to $+200$ MPa. These stresses can produce significant deformations on thin substrates, requiring either a modification of film or substrate design, or the use of post coating stress reduction techniques such as annealing (annealing, however, may cause diffusion across the interfaces, degrading reflectance).

Design, specification, and performance
Typical design constraints for an x-ray telescope will include focal length, spectral bandwidth, collecting area, resolution or fractional encircled energy, and size and weight. Not always independent of one another, these constraints determine whether a normal or grazing incidence telescope is desired, mirror figure requirements, coating design and element size.

Spectral bandwidth can determine whether an NI or a GI telescope is more appropriate. For extreme ultraviolet and very soft x-rays with wavelengths greater than $\sim$100 Å, NI multilayer telescopes offer lower cost, better imaging and larger collecting area. Spectral regions above 0.1 keV are better served by GI optics which offer much greater reflection efficiency and better performance.

Diffraction by the annular entrance aperture can be significant at low energies. The intensity as a function of radial position x is expressed as:

$$I(x) = \frac{4}{[1-(r_i/r_o)^2]^2}\left[\frac{J_1(x_o)}{x_o} - \left(\frac{r_i}{r_o}\right)^2\frac{J_1(x_i)}{x_i}\right]^2$$

where

$$x_o = 2\pi r_o\frac{x}{\lambda f} \qquad \text{and} \qquad x_i = 2\pi r_i\frac{x}{\lambda f} \tag{10}$$

where r_o and r_i are the outer and inner radii of the annular aperture, respectively, f is the focal length, J_1 is the first-order Bessel function and λ is the incident wavelength. For NI telescopes diffraction does not limit imaging performance until one produces extraordinarily precisely figured optics, as discussed above in the section 'Multilayer telescopes'. Depending on telescope size, aperture diffraction can be more significant for GI optics. For example, the X-Ray Telescope (XRT) on the joint US–Japan Solar-B satellite has an aperture width of about 0.6 mm and an outer radius of $\sim$170 mm. At a wavelength of 60 Å, the 68% point of the fractional encircled energy (the radial integral of the normalized point spread function)

is about 1.4 arcsec in diameter. For the large Chandra aperture diffraction is negligible.

Grazing angle, focal length and radius are related by the relation

$$\alpha = \frac{1}{4}\tan^{-1}\frac{r_0}{Z_0} \qquad (11)$$

where α is the graze angle at the intersection of the paraboloid and hyperboloid surfaces, and r_0 is the radius of the virtual joint (Z_0 is not the focal length but it is fairly close). The choice of graze angle affects the short-wavelength limit of the telescope because of the precipitous loss of reflection efficiency near the critical angle. Therefore spectral bandwidth coupled with focal length can drive the maximum allowable optic size. From these few parameters one can derive the optical prescription of the paraboloid and hyperboloid using the method of Van Speybroeck and Chase (1972). If we constrain the graze angle of the hyperboloid at the virtual joint to be 3 times that of the paraboloid, then the prescription of the optics can be determined as

$$P = Z_o \tan(4\alpha)\tan\alpha \qquad (12)$$

$$d = P \qquad (13)$$

and

$$e = \cos(4\alpha)[1 + \tan(4\alpha)\tan(3\alpha)] \qquad (14)$$

where the optical surfaces are represented as

$$r_p^2 = P^2 + 2PZ + 4e^2 Pd/(e^2 - 1) \qquad \text{paraboloid} \qquad (15)$$

and

$$r_h^2 = e^2(d + Z)^2 - Z^2 \qquad \text{hyperboloid} \qquad (16)$$

and Z represents the coordinate along the optical axis and is zero at the system focus and e is the eccentricity. The effective focal length of the system, fL, is expressed as

$$fL = \frac{2e^2 d}{e^2 - 1}. \qquad (17)$$

(The ratio of fL/Z_o is a function of α and is approximately equal to $1 + 0.0025\alpha_{\text{deg}}^2$.)

Typically, performance of GI systems is expressed in terms of the encircled energy (usually as a fraction or as a per cent). This is the integral of the point spread function within a given angular diameter. One can think of the encircled energy as the fraction of incident flux that falls on a detector pixel or some other suitable area (e.g. a slit for some spectroscopy applications). It is a measure of how compact or spread out the light from a point source is imaged. The encircled energy may be normalized or scaled two different ways. In the first, normalization is with respect to the flux that leaves the last focusing optic (reflection losses are ignored). In the second approach the normalized encircled energy is scaled by the entrance aperture area and has units of area.

Image quality is affected by mirror surface imperfections (figure error and microroughness) which scatter the

incident flux and broaden the point spread function. For conceptual purposes mirror errors may be loosely grouped into three categories. Low spatial error frequencies (long error periods) produce small-angle scatter which has only a small effect on the image 'core'. Mid-spatial-frequency errors produce intermediate-angle scattering and can have a significant effect on the image core, limiting resolution—the ability to discern two closely placed sources. High spatial error frequencies (typically microroughness) produce large-angle scatter (this might be on the order of 10–100 arcsec and greater) which degrades image 'contrast'—the ability to find a dim source in the presence of a bright source. The definition of what error frequencies correspond to the various bandwidths is dependent on the system requirements and grazing angle. On Chandra, errors that scatter x-rays by 0.5 arcsec would be considered mid-frequency. On XMM, mid-frequency errors might be considered as those that scatter by 5 arcsec.

A zeroth-order estimate of encircled energy can be made using the total integrated scatter, or TIS. This term represents the fraction of incident energy that is scattered by a surface (or equivalent surface) with a given rms surface figure error. The fractional encircled energy (or EE) is approximately $1 - $ TIS. The EE is both incident wavelength and included angle dependent, so the choice of rms figure error must take this into account. This is done by using a bandlimited rms amplitude and making the assumption that this amplitude includes all surface error frequencies that will scatter the light outside the desired region of interest. The encircled energy is expressed (approximately) as

$$\text{EE} \approx \exp[-(2k\sigma\sin\alpha)^2] \qquad (18)$$

where k is equal to $2\pi/\lambda$, σ is the bandwidth-limited effective rms surface error (in the plane of incidence) and α is the average graze angle. Using encircled energy goals we can estimate an acceptable value for σ, or, alternatively, σ can be used to estimate EE. (Of course, we want to leave some additional margin as we recognize that pointing stability–jitter, alignment, etc will all degrade performance.) To determine the bandwidth for which σ applies we use the grazing incidence equivalent of the grating equation (making use of the small-angle approximation)—

$$\lambda f = \theta_s \sin\alpha \qquad (19)$$

where λ is the incident wavelength, f is the spatial frequency of the surface error and θ_s is the angle through which the radiation is scattered. All errors of higher spatial frequency will scatter through larger angles and fall outside the region of interest. In doing this analysis we are mostly concerned with errors in the axial direction. This is because the deviation of specular rays out of the plane of incidence by azimuthal errors is reduced by a factor of $\sin\alpha$. Similarly, the scattering distribution is elongated in the plane of incidence by a factor of $1/\sin\alpha$ (the grazing incidence foreshortens the spatial error periods in the plane of incidence, making the errors appear as a

higher-frequency and increasing the scattering angle (see equation (19))).

A more exact method of computing telescope requirements and estimating performance is obtained using the scalar scattering theory of Beckmann and Spizzichino. (Vector scattering theory may also be used for modeling performance. Some references by E Church are listed in the bibliography.) The output intensity distribution is given as

$$\frac{\mathrm{d}P}{\mathrm{d}\Omega_{\mathrm{total}}} = \mathrm{Strehl}\,\frac{\mathrm{d}P}{\mathrm{d}\Omega_{\mathrm{spec}}} + \frac{\mathrm{d}P}{\mathrm{d}\Omega_{\mathrm{spec}}} \otimes \frac{\mathrm{d}P}{\mathrm{d}\Omega_{\mathrm{scatt}}}. \qquad (20)$$

Strehl is the Strehl ratio and equals the right-hand side of equation (18). $\mathrm{d}P/\mathrm{d}\Omega_{\mathrm{spec}}$ is the intensity distribution in the absence of scattering–diffraction, such as results from large-scale geometric figure and alignment errors, $\mathrm{d}P/\mathrm{d}\Omega_{\mathrm{scatt}}$ is the scattered intensity distribution and $\otimes$ signifies a convolution operation. Using scattering theory to determine $\mathrm{d}P/\mathrm{d}\Omega_{\mathrm{scatt}}$ and integrating over $\mathrm{d}\Omega$ yields the encircled energy. After much algebra this can be reduced to a one-dimensional integral where the scattering is a function of the Fourier transform of the optic axial figure error power spectrum density (PSD). Thus, by measuring the axial surface errors (i.e. the axial one-dimensional profiles), computing the error PSD and measuring the geometric in- and out-of-plane contributors, we can estimate performance. Initially appearing complex, this formalism is very useful because optic (and replication mandrel) fabrication processes are essentially surface filters. Imaging performance is a function of surface error PSD, and optical fabrication technology provides a means to operate on the surface error PSD. This approach provides much more fabrication guidance than merely specifying a single bandlimited rms amplitude as an optic requirement. This approach also correctly takes into account the impact of the frequency content of the figure errors in estimating performance.

Fabrication

Grazing incidence telescopes are produced by one of several methods: direct polishing of the optics, replication of polished mandrels or forming of thin foils. Multilayer telescopes are manufactured using standard precision optical fabrication methods but require the application of the multilayer coatings.

Material considerations for x-ray optics are important. Since all x-ray observations are made in space, the optical elements must be strong enough to survive rocket launch acoustic and seismic loads. At the same time, optic weight must be minimized to reduce payload weight. Depending on the complexity of the spacecraft an active temperature control system may or may not be present, so mirror elements should have both a low coefficient of thermal expansion (CTE) and a uniform one. This minimizes optic distortion due to temperature variations and gradients in the spacecraft as it orbits the Earth.

Typical glasses used for x-ray telescopes are Zerodur™, a glass ceramic produced by Schott with an extremely low CTE, and ULE™ (which stands for ultralow expansion) produced by the Corning Glass Co, another very low-CTE glass. Fused quartz was used for the Einstein Observatory mirrors. Potential new materials include silicon carbide which has an extremely high strength to weight ratio offering the promise of very light weight non-replicated optics.

Optical fabrication of grazing incidence optics
Optic blanks arrive from the glass supplier as rough machined pieces, within 250–1000 μm of final dimensions (by contrast, final allowable figure error might be only a few hundred Ångströms, rms, or 10^4–10^5 times better). A carefully scripted material removal schedule utilizing ever-finer grinding grits and polishing compound is used to coarse figure the optics and remove residual machining stresses (subsurface damage, or microcracks) that can degrade figure stability or even lead to catastrophic failure under load. The inside (optical surface), outside and ends of the blank are polished for damage removal, to provide a surface that is easily cleaned and kept free of contamination, and to provide a controlled bonding surface for the optic mounting system.

The optical surface is figured in (grinding and) polishing using computer-controlled fabrication technology where a computer provides a set of commands to move the polishing head in a controlled fashion over the surface of the optic. Typically, the optic is supported with its axis nearly horizontal, the optic is made to rotate about its axis at a controlled rate, and the polishing tool is driven axially along the optical surface to describe a fixed path (e.g. a spiral), but with variable path velocity. Since material removal is inversely proportional to the path velocity, control of that velocity allows correction of the optical figure. The velocity commands result from deconvolving the polishing tool material removal profile from the optic surface error map. The fabrication process, along with the associated measurements, is iterative with typical error correction rates of 50–90% per iteration depending on the optics manufacturer. For Chandra, the correction rates were typically 85–95% depending on the error spatial frequency content.

Smoothing of the optic, critical for controlling scatter, is usually performed as a separate operation from figuring. ROSAT optics were smoothed to surface roughness levels of about 3 Å, rms, and the Chandra optics were smoothed to about 2–3 Å, rms.

The combination of computer-controlled fabrication and smoothing function as spatial frequency filter operations, making them readily linked to the PSD requirements that can be generated from the encircled energy requirement.

Because of the unusual optic geometry, most fabrication and metrology equipment is custom designed by the manufacturer. For larger optics such as on ROSAT and Chandra specialized handling equipment is also required.

Fabrication of grazing incidence optics by replication
When extremely good imaging (less than a few arcsec diameter) is not required, or when extremely large collecting area is required, replicated optics can be a superior alternative to individually fabricated glass optics. In this approach a set of replication mandrels that are the inverse of the desired final figure are fabricated first. Multiple replicas, each the inverse of a mandrel and therefore possessing the desired mirror figure, are then formed.

The advantages of replication are several. First, when multiple copies of the same mirror are required, replication is cheaper and less time consuming than individually fabricating each mirror. Second, many more shells can be nested within one another (without unduly growing the size of the outermost elements) because the replicas are typically much thinner than glass elements. This results in higher telescope 'throughput'. Third, because of their relative 'thinness' replicated optics may weigh substantially less than corresponding glass elements, reducing payload weight. (As an example, the largest X-ray Multi-mirror Mission (XMM) replicated nickel optics are less than 1/4 the weight per unit axial length of the corresponding size Zerodur™ Chandra counterparts.) These advantages mean that either the instrument can carry multiple copies of the telescope optics and detector (such as XMM) or multiple identical satellites can be placed in orbit (such as planned for Constellation-X). Replication is a way to achieve much larger collecting area and higher telescope throughput with lower weight per unit area at less cost than with non-replicated elements.

The disadvantage of replication (to date) is the level of figure quality which may be achieved, limiting imaging performance to ~14 arcsec, half power diameter (or 50% encircled energy). The mandrels themselves may be fabricated with the same accuracy as large glass elements. The difficulty arises in attempting to remove the lightweight replica from the mandrel, maintain its figure against internal stresses created while producing the replica and then support it for flight, without introducing low spatial frequency distortions in the figure.

The strengths of replicated optics and individually figured optics telescopes such as XMM and CXO are complementary. Replicated telescopes, with their large collecting area and good imaging capabilities, are generally more useful for imaging spectroscopy. For bright objects, however, telescope throughput is not a limiting factor and the full imaging capabilities of glass optics can be brought to bear. Replicated optics are more suitable for some observations of very faint objects or deep sky surveys where the photon noise limit obviates finer resolution, but the limiting angular resolution may also result in an inability to resolve discrete sources. Alternatively, glass optic telescopes may be limited in the number of deep surveys possible owing to the extended observing time needed to collect enough photons necessary to make full use of their imaging.

Several methods of replication are briefly described below.

Nickel replicas An aluminum mandrel is coated with ~200 μm of electro-less nickel (Kanigen). The electro-less nickel surface is loose abrasive ground and computer-controlled polished or diamond turned to the nominal figure (after diamond turning additional figuring may be required). The surface is smoothed (polished) to about 5 Å, rms, roughness, to complete the mandrel. The replica is produced by first depositing 100–200 nm of gold on the electro-less nickel surface and then electroplating the gold with nickel to the desired thickness (~1 mm). The replica is separated from the mandrel by cooling the mandrel (the coefficient of thermal expansion for aluminum is about twice that of nickel). The gold coating separates with the nickel replica because its adhesion to the electroplated nickel is much greater than to the Kanigen. Multiple replicas may be made from a single mandrel before the mandrel needs to be refurbished. Replicas of this type have been used for the BeppoSAX, JET-X and XMM. Replica sizes range from 300 mm long, 68 mm diameter on BeppoSAX to 600 mm long, 700 mm diameter on XMM. The half-energy width of the point spread function at 1.5 keV is 13 arcsec for XMM.

As previously mentioned, internal stresses in the electroplated nickel will deform the replica when it is removed from the mandrel. Potential solutions to the lack of structural rigidity of these replicas include the use of stiffening structures fixed to the replica during the nickel plating process and the use of ceramics or silicon carbide (SiC) in place of the nickel replica substrate. In the latter approach the SiC substrate is formed to near final shape by chemical vapor deposition (CVD) to a second mandrel slightly larger (10^2 μm) than the first. The first mandrel is coated with 100 nm of gold, and then the SiC substrate is positioned around it. The gap is filled with epoxy, and, after curing, the gold-coated epoxy/SiC replica is separated from the Kanigen-coated aluminum mandrel by cooling. The CVD SiC has little residual internal stress and has a Young's modulus approximately 3 times larger than that of nickel. The SiC replica can be made substantially thinner than the nickel replica. A similar process using a beryllium substrate instead of SiC has been used on the Exosat program. An alternative approach in which aluminum oxide is plasma sprayed directly on the gold-coated Kanigen/aluminum mandrel is also under investigation at the time this article is being written.

Epoxy replicas In epoxy replication an aluminum foil serves as the replica substrate. A glass (Pyrex™ or Zerodur™) mandrel is coated with ~100 nm of gold. A thin (~100 μm) aluminum foil is pre-formed to the approximate shape of the coated mandrel but slightly oversized. Both the gold-coated mandrel and the (inner) surface of the foil are sprayed with epoxy and the two are then mated. The epoxy film, several tens of microns thick, is cured in an oven before the foil is removed. The foil maintains the smoothness of the polished glass mandrel. Epoxy replicas have not at this time achieved the imaging capabilities of nickel replicas, but the replicas

Table 1. An abbreviated list of some of the more notable x-ray telescopes.

Mission	Type	Effective area (cm^2)	Resolution (HPD, arcsec)	Energy bandwidth[a] (keV)	Comments
Skylab (1975)	GI	42 (collecting area)	~2 arcsec resolution	0.2–2	First x-ray telescope; solar observations
Einstein Observatory (1978–81)	GI	~200 at 1 keV	~15	0.2–4.5	First telescope observatory; discovered 7000+ sources
RXRS[b] (1987)	NI	~50 (collecting area)	~2 arcsec resolution	17.3, 25.6 nm	First NI solar telescope(s); 6.3 cm diameter primary mirror
ROSAT (1990–9)	GI	400 at 1 keV	~5	0.1–2.4	4 Au coated Zerodur shells; discovered 150 000+ sources
ASCA (1993)	GI	1300 at 1 keV, 600 at 7 keV	174	0.5–10	Conical foil Al mirrors, Au coat over lacquer, 4 separate telescopes
BeppoSAX (1996)	GI	330 at 1 keV	60	0.1–10	Nickel-replicated conical optics, 30 nested shells
TRACE (1998)	NI	~20	1	17, 20, 28 nm	30 cm diameter primary, 2 m focal length solar telescope
Chandra (1999)	GI	800 at 1 keV	0.5	0.1–10	Highest resolution, 4 shells, largest mirror 1.2 m diameter transmission gratings
XMM (1999)	GI	4650 at 1 keV, 1800 at 8 keV	14	0.1–12	Nickel replicas, 3 telescopes, 58 shells each, reflection gratings
Constellation-X (200?)	GI	15 000 at 1 keV 1500 at >6 keV	15 (<10 keV) 60 (>25 keV)	0.25–10, 6–40	Replicated optics (type to be determined), ~80+ shells, largest 1.2 m diameter grating

[a] For NI telescopes the tabulated values represent the approximate centers of the reflection bandpass(es).
[b] Stanford University/NASA Marshall Space Flight Center Rocket X-Ray Spectroheliograph.

are substantially lighter owing to their much thinner wall and less dense substrate material. To date limiting performance is ~1 arcmin.

Segmented foil replicas Segmented foil mirrors have been used on the Broad Band X-Ray Telescope (BBXRT), ASCA and the Sodart telescope on board SPECTRUM-X-GAMMA. Here the mirrors do not form the complete surface of revolution, but instead form (typically) only a single quadrant. Aluminum foils less than a millimeter thick and optically smooth are rolled into a 90° section of the desired conical shape (note that the mirrors, being true cones, are only approximations to Wolter I telescopes). Plastic deformation (rather than elastic bending) is employed to produce a final shape that more closely approaches the nominal and does not introduce stresses into the support structure. After rolling, the foils are dip-coated with an acrylic lacquer to improve (reduce) scattering due to surface roughness. Care is taken to avoid introducing variations in lacquer thickness that would change the optical shape of the mirror, degrading imaging. Mirrors of this type are very inexpensive to produce but have not achieved better than a few arcminutes resolution. In part

this limitation is a result of the approximation to a Wolter I system, but, more importantly, it appears that the lacquer is ineffective at smoothing errors with spatial periods greater than a few microns. These errors significantly affect the ability to image at better than the 1 arcmin level.

Fabrication of normal incidence multi-layer telescopes
Normal incidence x-ray multilayer telescopes are essentially manufactured using the same processes as conventional precision optics with two major exceptions: optic smoothness (or microroughness), which affects both scatter and multilayer reflectivity, and the deposition of the x-ray multilayer coating.

As discussed above in the section 'Reflection from multilayer coatings' reflectance is a function of high spatial frequency roughness ($f > 10^3$ mm^{-1}). Super-smoothing of the surface roughness in this very high spatial frequency regime to levels of 2–4 Å, rms, is necessary for good reflectance.

Along with substrate roughness, the multilayer coating is the most critical element of the optics. To achieve the desired reflectance over the correct spectral bandwidth requires uniformity of coating thickness both across the face of the optic as well as from layer to layer. Coating

density must also be uniform throughout the multilayer. In addition, interlayer diffusion must be minimized as must thin-film stresses.

Telescope systems

Other parts of a telescope system are the detector, optical bench and mirror mount or support structure. CHARGE COUPLED DEVICES (CCDs) have supplanted position-sensitive proportional counters. CCDs may be either front or back illuminated. Front-illuminated CCDs have the x-rays impinge upon the semiconductor gate side. Back-illuminated CCDs have additional wafer processing to thin the backside of the chip (the side away from the gates) and are then set so that the x-rays impinge upon the backside. Front-illuminated CCDs provide better energy resolution and slightly higher quantum efficiency at high energy than back-illuminated CCDS. Back-illuminated CCDs provide substantially higher low-energy x-ray quantum efficiency. A wide range of pixel sizes are available: the Chandra CCDs have 24 μm pixels; the Solar X-ray Imager (SXI) on GOES N and O will have ~15 μm sized pixels. The long focal length (~10 m) of Chandra coupled with 24 μm pixels yields ~0.5 arcsec angular resolution. CCDs provide excellent energy resolution, about 120 eV for the Chandra detectors. Several CCDs may be arrayed to cover the full field of view of the telescope, and the detectors may also be arrayed so as to be aligned to the curved focal surface, thereby eliminating focus error that occurs with a flat detector and a curved focal surface (see equation (6)). Higher imaging resolution is achieved with less energy resolution using detectors such as the Einstein, ROSAT and Chandra High Resolution Imager. This is a pair of stacked multichannel plates with an electronic readout. Future developments include the use of microcalorimeters, which will be used for the first time on Astro-E. This device has an energy resolution of ~12 eV at 6 keV but has a relatively large pixel size and so limits spatial resolution. Spectroscopy with x-ray telescopes is also accomplished by the use of transmission gratings that may be moved in and out of the focused beam, such as on Chandra, or reflection gratings fixed in the beam as on XMM.

X-ray telescope missions

Some significant x-ray telescopes and performance details are listed in table 1.

Future trends

In grazing incidence telescopes future trends will continue the development of increased collecting area, improving resolution and increasing reflectance. The use of ceramics and SiC, including the use of monolithic support structures, will improve the limiting performance of what used to be nickel mandrels, while also allowing denser nesting of mirror shells. Researchers have been experimenting with the application of broadband multilayer coatings to grazing incidence optics, increasing reflectance at higher energies. With respect to normal incidence telescopes future development will probably focus on achieving diffraction limited performance with increased focal lengths to more fully utilize the improved optics.

Bibliography

There are a multitude of excellent articles in the literature discussing the technology of x-ray telescopes. For design issues of GI telescopes one is referred to

Van Speybroeck and Chase 1972 Design parameters of paraboloid–hyperboloid telescopes for x-ray astronomy *Appl. Opt.* **11** 440

An excellent review is found in

Aschenbach B 1985 X-ray telescopes *Rep. Prog. Phys.* **48** 579

Discussions of alternative Wolter-I-like designs with improved off-axis performance can be found in

Nariai K 1987 Geometrical aberration of a generalized Wolter type I telescope *Appl. Opt.* **26** 4428
Werner W 1977 Imaging properties of Wolter I type x-ray telescopes *Appl. Opt.* **16** 764

Atomic scattering factors for computing reflectance are found in

Henke, Gullickson and Davis 1993 *At. Data Nucl. Data Tables* **54** (2)

This information is also available on the Wide World Web at URL

http://xray.uu.se/hypertext/henke.html.
A second site,

http://www-cxro.lbl.gov:80/optical_constants
contains the same data along with a reflectance 'calcula-tor'. A general review of multilayer coatings can be found in

Barbee 1990 Advances in multilayer x-ray/EUV optics: synthesis, performance, and instrumentation *Opt. Eng.* **29** 711

Discussions of vector and scalar scattering theory are reviewed by

Church E 1979 Role of surface topography in x-ray scattering *SPIE Proc.* **184** 196
Church E 1986 The interpretation of glancing incidence scattering measurements *SPIE Proc.* **640** 126

For more detailed discussions of developments the reader is best referred to the Society of Photo-Optical Instrumen-tation Engineers (SPIE) annual proceedings for grazing incidence and multilayer x-ray optics. Some recent vol-umes are *SPIE Proceedings* volumes 3444 (published in 1998), 3113 (1997), 2808 and 2805 (1996) and 2515 (1995).

Paul B Reid